Research Article Vol. 31, No. 10 / 8 May 2023 / Optics Express 17027

Optics EXPRESS

Refractive-type varifocal liquid-crystal Fresnel lenses for smart contacts

AISHWARYADEV BANERJEE,[†*] CHAYANJIT GHOSH,[†] MOHIT U. KARKHANIS, ADWAIT DESHPANDE, ERFAN POURSHABAN, APRATIM MAJUMDER, HANSEUP KIM, AND CARLOS H. MASTRANGELO

Department of Electrical and Computer Engineering, University of Utah, Salt Lake City, Utah 84112, USA
[†] Authors have equal contribution.
[*] *devaash88@gmail.com*

Abstract: We demonstrate the implementation of a low-power, low-profile, varifocal liquid-crystal Fresnel lens stack suitable for tunable imaging in smart contact lenses. The lens stack consists of a high-order refractive-type liquid crystal Fresnel chamber, a voltage-controlled twisted nematic cell, a linear polarizer and a fixed offset lens. The lens stack has an aperture of 4 mm and thickness is ~980 µm. The varifocal lens requires ~2.5 V_{RMS} for a maximum optical power change of ~6.5 D consuming electrical power of ~2.6 µW. The maximum RMS wavefront aberration error was 0.2 µm and the chromatic aberration was 0.008 D/nm. The average BRISQUE image quality score of the Fresnel lens was 35.23 compared to 57.23 for a curved LC lens of comparable power indicating a superior Fresnel imaging quality.

1. Introduction

The aging of the eye crystalline lens results in the inability to focus clearly on objects. This condition, also known as presbyopia, currently affects more than 1.8 billion people worldwide and is also a major cause of accidental injuries in the elderly [1]. The average accommodation range drops from 11 diopters (D) on 20-year-olds to < 2 D by the age of 50 [2].

Currently, presbyopia is treated using corrective devices such as multifocal and progressive eyeglasses, contact lenses and intra-ocular lenses. However, such solutions provide zoned fixed optical power offsets, and none of them restore accommodation. These devices essentially partition the aperture into different focal zones significantly reducing the effective field of view resulting in visual impairment.

Alternate to the zoned approach, one can utilize adaptive optics-based solutions for presbyopia correction. Recently there has been a surge in efforts to develop and deploy smart autofocusing eyeglasses which comprise of adaptive tunable lenses that can automatically focus on the object of interest [3–7]. However, in its current form, due to their inherent requirement of very large aperture tunable lenses, autofocusing eyeglasses suffer from several problems. Some of these are bulky for daily usage while others have a reduced aperture or produce other undesirable aberrations. Their form factor, weight and physical appearance are major social barriers as users expect accommodation-corrective eyeglasses that look and feel like their fixed power counterparts.

A more compact and elegant solution that overcomes these social barriers is a smart contact lens (SCL) that can confirm to the eyeball and provide adaptive optical accommodation and clear vision to the user without changes in their physical appearance. Although there is significant research and technology development being carried out in the field of SCL technology, most of these cater to applications related to artificial iris for vision correction [8], AR/VR displays, drug

#489093
Journal © 2023
https://doi.org/10.1364/OE.489093
Received 3 Mar 2023; revised 14 Apr 2023; accepted 18 Apr 2023; published 5 May 2023

delivery [9], glucose detection [10] and eye comfort [11]. In this paper, we focus on an SCL technology aimed at vision correction specifically for individuals suffering from presbyopia.

2. SCL microsystem requirements

An adaptive SCL microsystem should consist of a scleral eye-tracking distance ranger [12–14], a compact energy source [15–19] and most importantly, an electro-optical tunable lens which provides different distance-dependent optical powers [20], [21]. For this application, the tunable lens must consume very little power yet provide adequate accommodation (~4D) with low actuation voltages. Additionally, a typical eye-mounted SCL platform has a very small, non-planar or fractured (origami) planar substrate area (~5 cm^2) available for placing all required components and interconnects hence severely limiting the number of electrical connections that can be realized on the substrate.

In particular, the most severe constraint for this application emerges from the power system storage capability. For example, even when utilizing 50% of the available substrate area for thin (~200 μm) Li batteries with an energy density of ~1500 MJ/m^3, the SCL energy storage is limited to ~75 J, which translates to an average total power delivery of 1.7 mW over a 12-hour operation period. Utilizing a microcontroller-compatible SCL voltage of 3.3 V, this translates to an average system current consumption of ~500 μA available to run all systems in the SCL. In practice the battery will be smaller; hence we set ourselves a target current of 150 μA with 50 μA allocated for the tunable lens operation and the rest for the other SCL subsystems.

3. Varifocal lens selection

Based on the above system and electrical power constraints, many common tunable lens technologies simply cannot be used for this application. For our purpose, polarization-dependent liquid-crystal (LC) tunable lenses at first appear very appealing due to their very low electrical power (~30 $\mu\text{W/cm}^2$ @ 1 kHz pulsed drive) operation [22], [23]. The low electrical power is attributed to the LC lens tunability mechanism based on electric field induced molecular rotation. This mechanism contrasts with many others that require macroscopic mechanical deformation and/or fluid transport requiring higher energy and power consumption.

LC lenses are polarization dependent beam shaping elements with optical power that can be controlled by an external electric field (magnitude, frequency or duty-cycle of the voltage source), magnetic field, or by simply changing the polarization of the incoming light. A birefringent LC has a linear polarization-dependent effective index of refraction n_{eff} given by:

$$n_{eff} = \frac{n_e n_o}{[n_o^2 cos^2\Phi + n_e^2 sin^2\Phi]^{\frac{1}{2}}} \tag{1}$$

where Φ is the angle between the LC director vector and the polarization of the incident light [23], [24] and n_e and n_o are the extraordinary and the ordinary refractive indices of LCs, respectively. For a refractive varifocal LC lens enclosed in a plano-convex cavity of wall index n_w and curvature radius R, the polarization angle dependent optical power and maximum optical power change are:

$$P(\Phi) = \frac{1}{R} \cdot \left(\frac{n_e n_o}{[n_o^2 cos^2\Phi + n_e^2 sin^2\Phi]^{\frac{1}{2}}} - n_w \right), \qquad \Delta P_{max} = \frac{1}{R} \cdot (n_e - n_o) \tag{2}$$

Note that the maximum power change depends on the difference between the ordinary and extraordinary LC indices which is ~0.17 for 5CB for example. This low-index difference essentially determines the required lens curvature radius. The fundamental light modulation mechanism of a nematic LC is electric field-induced molecular reorientation which, in turn, causes refractive index change [25]. Nematic LCs require a minimum electric field and voltage thresholds [26] for electric field induced realignment. A thicker lens thus requires a higher operation voltage.

LC lenses have been considered for low-power imaging applications elsewhere [23], [27–29], but these lenses in general suffer from LC-induced scattering which severely impacts imaging quality [30–33]. Light scattering is very pronounced for LC layer thicknesses >50 µm and optical images recorded through thick LC lenses appear cloudy with scattering increasing exponentially with thickness [34]. Image quality can be somewhat improved by digital signal post-processing [30], [31], but this is not an option for SCL eyewear application. The utilization of thinner LC layers leads to better image quality. In a plano-convex lens the aperture radius a, lens curvature radius R and height h are connected by the relation

$$h = R - \sqrt{R^2 - a^2} \approx \frac{a^2}{2R} = \frac{a^2\,\Delta P_{max}}{2(n_e - n_o)} \tag{3}$$

A thin plano-convex lens results in either a reduced tunability or a very small aperture for this application (SCL for presbyopia correction requires ΔP_{max}~4D change and aperture size of ~4 mm).

The need for both high optical power tunability and thin LC layers is thus not satisfied well with conventional refractive plano-convex geometries. It is better satisfied with LC Fresnel-type lenses (LCF). Fresnel lenses are wavelength specific lenses constructed by dividing a curved refractive lens geometry into a set of thin concentric annular sections with ridged grooved steps between them. The thin annular sections are obtained by hollowing out the lens sections that produce phase delays of integers of 2π and collapsing the remainder. In the m^{th}-order Fresnel, the ridges occur when the lens phase delay is equal to $2\pi m$, yielding a lens height $h(m)$

$$h(m) = \frac{m\lambda_o}{(n_{eff}(\lambda_o) - 1)} \tag{4}$$

where λ_o is the lens design wavelength (~0.5µm). Since for LC layers n_{eff} ~1.5 then the minimum ridge height for $m = 1$ is about twice the design wavelength. The very thin height essentially eliminates the LC light scattering issue, but a different problem emerges when we try to focus broadband light through the lens. Since the hollowing out procedure is done at a specific design wavelength, at other wavelengths the optical power of the Fresnel significantly diverges from its design value and, for low m, it causes large chromatic defocusing.

Fresnel lenses demonstrate a combination of refractive and diffractive optical behavior [35]. The groove ridges cause multiple diffraction order peaks and the loss of focusing efficiency, while the smooth areas between ridges are responsible for refractive focusing. The Fresnel lens thickness is key to the refractive/diffractive dominant behavior and the lens chromatic defocusing or chromatic aberration (CA). Mainly refractive thicker Fresnel lenses with few ridges have much less CA than thinner, high ridge density more diffractive Fresnel's [36]. This is discussed in the sections below.

4. Varifocal LC Fresnel lens design

For the SCL we thus seek a varifocal liquid-crystal Fresnel (VLCF) lens design that provides reasonably good imaging quality suitable for reading and distance focusing. There are many implementations of VLCFs found in the literature [37] as shown in Fig. 1, but not all of them are suitable for the SCL. Flat VLCFs (Fig. 1(a)) can be generated synthetically on thin uniform LC films through a complex set of concentric rings. electrodes and bias voltages [38], [39]. VLCFs can also be formed by LC-filling of grooved cavities (Fig. 1(b)) [21], [40] . The HPE voltage tunability feature at first seems attractive, but the wire routing of many electrodes and the generation of many analog voltages on the SCL substrate makes the layout difficult and the drive electronics complex. Furthermore, the low operating voltages (1.9-3.3 V) of ultralow-power driving microcontrollers and the electric field magnitude required to rotate the LC molecules limit the LC thickness to just a few microns thus resulting in large chromatic defocusing [36]. Therefore, we have selected a grooved-cavity type VLCFs instead. In these non-planar, oddly shaped lenses, the LC thickness is not uniform; hence it is not possible to continuously control the LC index of refraction with just one set of electrodes [41]. These lenses can only provide bifocal optical power settings (low, high) at the two extremes of the birefringence [42].

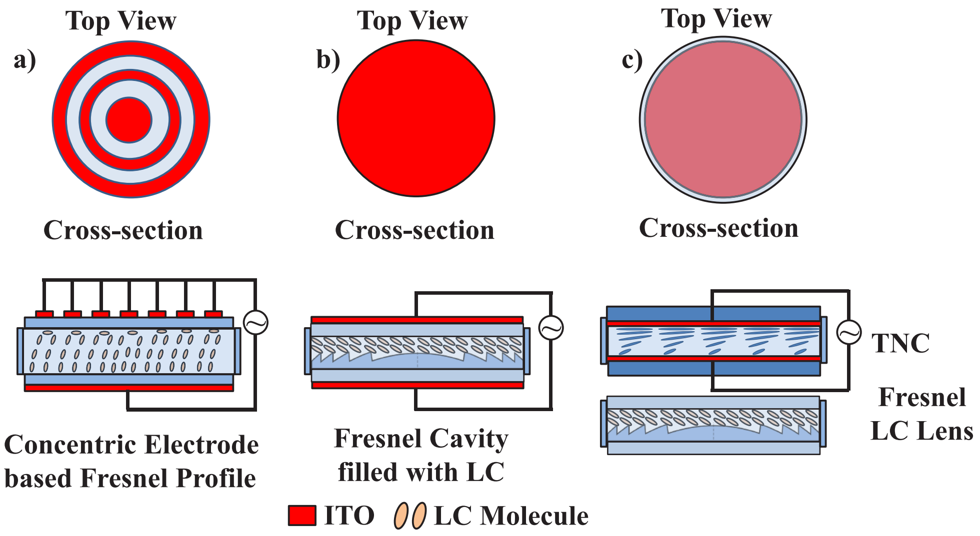

Fig. 1. Different implementations of varifocal LC Fresnel lenses: (a) synthetically generated flat LC lens via concentric electrode design and voltage shaping; (b) lens formed by filling a Fresnel grooved cavity with LC; (c) varifocal lens formed by stacking of LC grooved cavity and a low-voltage twisted nematic cell (TNC). The TNC rotates the polarization of the light before entering the grooved cavity.

Improved lens tunability can be achieved by elimination of the LC cavity electrodes and stacking of an additional thin (~3 µm), voltage-controlled twisted nematic cell (TNC) as shown in Fig. 1(c). The LC orientation in the grooved cavity is thus fixed. Continuous optical power tunability is achieved through varying the TNC voltage that rotates the polarization angle of the incoming light Φ before passing through the LC lens cavity [43]. The grooved-LC + TNC combination thus provides a variable optical power with just two electrodes and a low operating voltage requirement (~3 V).

4.1. LC thickness and chromatic defocusing

In order to achieve the best image quality as possible, it is desirable to make the LC layer as thin as possible to avoid scattering and image cloudiness. However, thinner the Fresnel lenses, and by extension, the LC layer, worse is the chromatic defocusing; hence there is a fundamental tradeoff between scattering and defocusing. The chromatic defocusing (or chromatic aberration (CA)) is subject to both material dispersion (wavelength-dependent index) and diffractive effects from the groove steps. The thinnest type of Fresnel with order $m = 1$ is the most widely analyzed [36], [44]. In a conventional $m = 1$ Fresnel lens, the optical power change with wavelength is:

$$\frac{\Delta P}{P_o} = \frac{\Delta \lambda}{\lambda_o} \tag{5}$$

where $\Delta\lambda = \lambda - \lambda_o$ is the deviation from the design wavelength and P_o is the optical power at the design wavelength. For example, an order $m = 1$ Fresnel lens of 10-diopter power at 550 nm shifts to 7.25 diopters at a wavelength of 400 nm and 12.75 diopters at 700 nm. This power change causes severe CA, thereby significantly degrading the image quality.

The CA of the Fresnel however reduces (and imaging quality improves) significantly if the groove steps are larger with order $m >> 1$. If the steps are uniform, such Fresnel are called harmonic diffractive lenses of HDLs. HDLs exhibit a maximum change in optical power [38]

$$\frac{\Delta P}{P_o} \leq \frac{\Delta\lambda_{max}}{m \cdot \lambda_o} \tag{6}$$

Because m appears in the denominator, the CA is reduced by a factor of $m >> 1$. The CA is reduced because the optical power resets to the design value P_o at multiple wavelengths. A large $m > 10$ thus reduces most of the CA effects of the grooves. The CA can be reduced even further with the incorporation of specialized diffractive elements [45] but this is beyond the scope of this work.

In this paper we seek VLCF design parameters that minimize the adverse impact of CA and scattering. As mentioned before, while increasing the groove height reduces CA, it also increases the lens thickness, thereby producing more LC-induced scattering of light. Both CA and scattering dispersion affect the overall MTF in a complex way. The overall MTF is approximately the product of the MTF due to CA and the MTF due to scattering.

$$MTF \approx MTF_{CA} \cdot MTF_S \tag{7}$$

The MTF due to CA can be obtained from the equivalent defocused MTF [46] while the scattering MTF strongly depends on the thickness and scattering coefficient of the LC medium [31]. The optimum m can then be obtained that gives the broadest MTF.

In practice this optimization procedure requires Fresnel surfaces of custom m which are expensive. Common off-the-shelf Fresnel lenses that can be used as molds typically come with fixed groove densities of 250 grooves/inch or 400 grooves/inch, depending on the baseline optical power required [47]. For our application we utilized 50D and 25D commercial Fresnel lenses, with a fixed groove density of 250 grooves/inch as molds for the LC cavity. In a fixed pitch groove-density Fresnel design, the height of the grooves is not uniform, increasing almost linearly with the distance from the lens center. This is because most Fresnel phase profiles are achromatic curves, such as a parabolic shape. The CA for this stepped ridge profile does not fit Eq. (5) or (6), but it can be solved numerically through the Huygens (or simplified Fresnel) integral [44] for circular aperture, axisymmetric phase profiles. The CA can be computed easily from the calculated intensity at the center of the lens versus distance z away from the lens. For a plane wave of amplitude A_o, the complex amplitude of the light transmitted by the lens can be calculated from the Fresnel integral of Eq. (8).

$$A(z,\lambda) = \frac{2\pi \exp(ikz)}{i\lambda z} \cdot \int_0^{r_a} A_o \exp(i\theta(r,\lambda))\exp(\frac{i\pi}{\lambda z} r^2)\, rdr \tag{8}$$

where r_a is the aperture radius and $\theta(r,\Phi,\lambda)$ is radius-dependent phase retardation introduced by the lens material:

$$k = \frac{2\pi}{\lambda}, \qquad \theta(r,\lambda,\Phi) = \frac{2\pi\,(n(\Phi,\lambda)-1)}{\lambda} \cdot h(r). \tag{9}$$

The normalized intensity transmission is thus,

$$I_n(z) = \left\| \frac{A(z)}{A_o} \right\|^2 \tag{10}$$

The normalization works for any arbitrary incoming plane wave; thus, for simplicity, we set $A_o = 1$. The one-dimensional integral of Eq. (8) is readily calculated numerically for any phase radial retardation profile $\theta(r,\Phi,\lambda)$ for a range of z using the python *numpy* package, as it can directly handle quadrature of complex numbers. The location of the main focal point f is numerically determined as the z point where I_n is maximum.

Figure 2 shows a comparison of the theoretical CA for acrylic Fresnel lenses (used as a mold for the LC cavity) for $m = 1$, $m = 5$, $m = 20$ and a fixed groove pitch lens (250 grooves/inch) all using quadratic aspherical profiles and design optical power $P_o = 50$D. Note that for the HDL Fresnel the CA curve shows a periodic ramp behavior while for the fixed-pitch Fresnel the steps in the ramps are not uniform. The results of the calculations indicate a standard deviation of the optical power of 8.7D, 3.9D, 0.95D and 0.87D respectively. The CA for fixed pitch Fresnel is dominated by the outer, taller grooves with CA in the same order as Eq. (6). When these Fresnel surfaces are utilized to cast VLCF lenses, the characteristics of the VLCF follow the same step characteristics with a reduced ΔP_{max} of about 1/8th of that shown in Fig. 2 above when using the birefringent LC 5CB [48], in the ballpark of the value needed for the SCL. For this paper we selected the fixed pitch Fresnel with aperture of 4.0 mm and groove density of 250 ridges/inch which has a maximum height of about 30 µm at the edge.

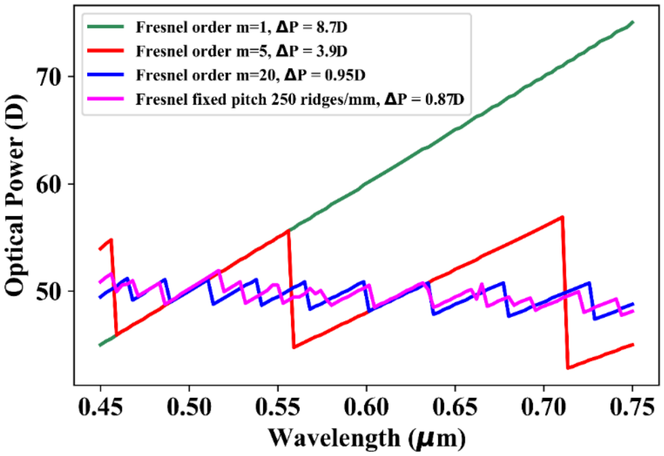

Fig. 2. Calculated chromatic aberration defocusing versus wavelengths for $m = 1,5,20$ and fixed pitch Fresnel lenses on acrylic. Note that the CA is very large for the thinnest $m = 1$ lens while for the higher order $m = 20$ and the fixed pitch the CA standard deviation is about 2% of the target power.

Figure 3(a), (b) shows a schematic of the final implemented VLCF lens system consisting of three stacked optical elements. The incoming light first passes through a linear polarizer film only letting through uniform linearly polarized light of a specific angle. The light exiting the polarizer is next passed through by a flat, very thin orthogonally twisted nematic LC cell (TNC). The TNC acts as a voltage-controlled polarization rotator [21], [36] that provides the optical tunability of the Fresnel LC lens through Eq. (2). The voltage-controlled TNC is basically a parallel-plate chamber, with a circular aperture, featuring an ultra-thin polyimide alignment layer (50 nm) and very thin 5CB LC layer of ~3 µm with twisted alignment. The combined thickness of the stack is ~0.98 mm. Figure 3(c) shows the assembled VLCF stack on a curved flex-PCB SCL platform. More details regarding the individual components forming the stack composition are provided in section 5.1. In the sections below we present the fabrication, testing and extensive characterization of VLCF lenses.

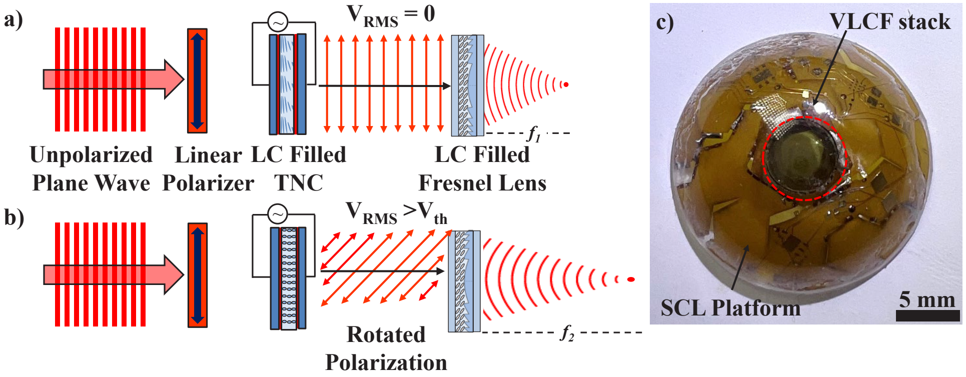

Fig. 3. (a),(b) Fundamental working principle of the VLCF system. By subjecting the TNC to a voltage > V_T (threshold voltage) one can change the focal length or optical power of the VLCF system. (c) Fully assembled fixed-pitch VLCF stack on an SCL PCB platform.

5. Methods and materials

5.1. VLCF flex PCB cap design and assembly of SCL platform

A two-layer flex-PCB (VLCF-cap) is used as a substrate for mounting the VLCF stack on another flex-PCB (SCL platform) and electrically connecting it to the rest of the SCL components. The thickness of the SCL platform was 80 µm, including a copper trace thickness of 18 µm. The SCL platform PCB layout was designed using a simple cut and fold origami technique that when assembled forms a partial Goldberg polyhedron [49] shell approximating a spherical cap. For permanent folding of the faces, small protrusions or 'tabs' were designed to be added to the edge of the cut faces which sported copper pads. Similar pads were also present on the opposite face sharing the edge with the faces with tabs, albeit with small holes. Copper pads were also placed on the bottom side of this face, under the holes to facilitate multilevel electrical connection. Solder was reflowed on the copper pads of the tabs. The two opposite edge sharing faces were brought in proximity such that the tabs rested underneath the holes. Heat was applied through the holes and the tab was solder-joined to the opposite face. Fixing all such tabs results in a curved, dome-shaped PCB in the shape of a scleral contact lens. The flex-PCB before and after folding is shown in Fig. 4(a), (b). The top of this flex-PCB is sliced during design to define the aperture of the lens and allow for proper placement of the VLCF stack. This is the SCL platform which will potentially comprise of all the components of the smart contact lens. However, in this article, we will only describe the fabrication and assembly/integration of the VLCF stack with the SCL platform. To facilitate proper electrical connections between the SCL platform and the TNC, the two-layer VLCF cap was fabricated which will be hereby denoted as L1 (170 µm thick) and L2 (140 µm thick). As shown in Fig. 4(c), L1 is a pentagon shaped PCB with carefully placed copper pads for electrical connections and L2 is another flex-PCB slab also featuring copper pads for multilevel electrical connections. Now, the PCB is ready for integration with the TNC and VLCF.

5.2. Fabrication of refractive Fresnel lens and TNC, and assembly on SCL substrate

Figure 4(d), (e) shows the fabrication flow of the LC filled refractive Fresnel and TNC chamber. The following sub-sections describe the details of the fabrication and assembly of the individual components of the VLCF stack.

Fresnel lens chamber fabrication and LC filling

A commercially purchased refractive Fresnel lenses with an optical power of 50D (hereby referred to as the base power of the VLCF) (Edmund Optics #13-458) was utilized as starting

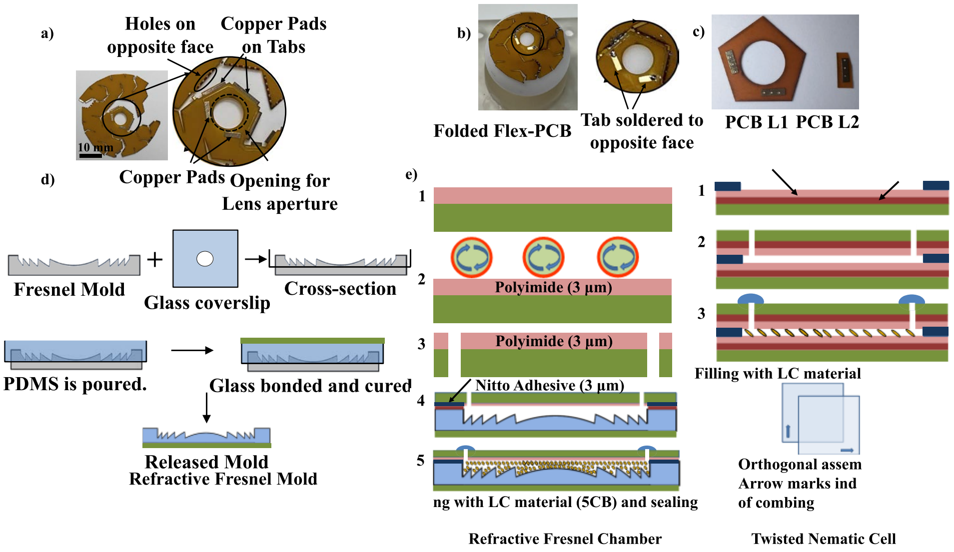

Fig. 4. (a) Optical image of the fabricated unfolded flex-PCB with an opening for the lens aperture. (b) Proper folding and attachment give a dome-shaped curved SCL platform which is shown mounted on a spherical platform. (c) L1 and L2 flex PCB collars for facilitating proper multilevel electrical connections between the TNC and the SCL platform. (d) Fabrication of the Fresnel chamber using contact molding of PDMS and (e) detailed steps for fabrication of VLCF lens and TNC chamber.

molds. These lenses were coated with a thin layer of Fluoropel (Cytonix Fluoropel 800 1%) to ensure easy and proper release of cured PDMS. The aperture of the lens was defined by a CO_2 laser cut (Universal Laser System Retina Smelter 9001) thin glass coverslip (WVR), placed on the mold and a fixed volume of PDMS (0.1 ml), mixed in the ratio of 1:6 (curing agent: base elastomer) was poured on the mold. The glass coverslip also acts as a rigid frame for the PDMS structure. Next, another uncut, Fluoropel coated glass coverslip was added on top to ensure a flat surface of the final cured PDMS structure. In absence of this coverslip, a slight free-forming curvature of the PDMS structure was observed, which led to unwanted optical characteristics and distorted waveforms. The other side of the PDMS confirmed to the Fresnel grooves and provided perfect replication. The PDMS was cured at 100°C on a hot plate for 2 hours. After curing, the coverslip structure with the Fresnel replicated cured PDMS was cleanly removed from the commercially purchased Fresnel mold (Fig. 4(d)). Finally, a roller conformally covered with locally purchased rayon cloth was used to physically comb the PDMS structure, to ensure proper alignment after filling the Fresnel chamber with LC. Typically, mechanical combing on PDMS leads to a very high vertical alignment and near 90° LC director pretilt angle w.r.t the PDMS surface [50]. However, due to the near vertical PDMS Fresnel groove structures, proper combing on PDMS finally leads to parallel LC director alignment w.r.t the glass coverslip plane.

Next, a thin layer (<2 µm) of Polyimide (PI2555) was spin-coated and properly cured on another glass coverslip of similar thickness. Mechanical combing using the rayon cloth covered roller was again performed on the spin-coated PI to ensure near 0° director alignment, w.r.t the PI thin-film. The PDMS Fresnel structure, along with the glass frame was attached with the PI coated glass coverslip using a commercially available very thin (∼3 µm) and optically transparent double-sided adhesive tape (Nitto Denko Corporation NO:5600). Finally, two very small holes (∼100 µm diameter) were laser cut into the PI coated glass coverslip for the final filling of LC material. After proper attachment, the entire chamber assembly was cut, keeping a circular opening of 5 mm at the center (to define the entire lens) and a very thin layer of silicone glue (Dowsil 734) was applied on the edges of the lens to prevent any leaking of LC liquid. Nematic LC material (5CB, purchased from Millipore Sigma) was carefully dispensed on the lens structure (ensuring that the dispensed LC material completely covers the holes). The entire assembly was then placed inside a desiccator and the LC was then vacuum filled. The volume of LC required to completely fill the Fresnel chamber was calculated to be ~0.2 µL. The pressure of the desiccator chamber was maintained at 570 Torr using a commercially purchased vacuum oil-pump. The filling time typically depends on the volume of chamber to be filled, and we typically required ~4 hours for filling the refractive Fresnel chamber. After filling, the lens was carefully taken out of the chamber and after proper and careful cleaning, the holes were sealed-off using ~3 mg of commercially purchased low-profile glue (Dowsil 734 clear flowable sealant) (Fig. 4(e)).

TNC chamber fabrication

As shown in Fig. 1(c), the twisted nematic cell or TNC, is simply a parallel-plate chamber, filled with LC material. A thin layer of ITO (~110 nm) is sputter-deposited on two glass coverslips. Next, a very diluted solution of PI was spin-coated on the ITO coated side of the glass structure. Detailed information regarding PI dilution has been provided here [51] and it essentially involves diluting the PI2555 material with N-Methylpyrrolidone (NMP) solvent in the ratio of 1:2 (wt/wt), followed by stirring at 500 rpm for 2 hours at room-temperature. This mixture was spin-coated on the glass coverslip at 4000 rpm for 60 seconds. The sample was then soft-baked at 90°C and 100°C for 1 minute and then baked at 300°C for 3 hours in a nitrogen environment oven. Complete details of the curing procedure have been described before and can be found here [52]. The final thickness of this PI layer was ~ 50 nm which was determined to ensure low threshold switching voltage of the TNC. Although lower thicknesses of PI would further lower the operating voltage, but such ultra-thin PI films are typically non-uniform in thickness and are susceptible to peel-off during subsequent combing steps. After curing, the PI layer was patterned using O_2 plasma RIE process to expose the underlying ITO. A very thin layer of copper (~200 nm) was sputter-deposited on the exposed ITO for facilitating eventual electrical connections. Finally, the PI layer was lightly combed using a rayon cloth covered roller for ~0° LC director alignment. It is important to note that these ultra-thin PI films are highly susceptible to scratching induced peel-off, therefore each sample was carefully inspected after the combing procedure under a high-resolution optical microscope (Keyence VHX 5000) to ensure the integrity of the thin-film before further assembly.

Two such PI/ITO deposited glass coverslips were cut into appropriate shapes to confirm to the flexible PCB design of the SCL platform. Two small holes (100 µm diameter) were etched into the top glass substrate using the CO_2 laser. The coverslips were orthogonally attached using a ~3 µm thick double-sided Nitto adhesive tape. This tape also served as a uniform spacer between the glass structures. The reference directions were considered parallel to the combing direction. It is important to note that critical to TNC performance is the orthogonal alignment of the combed PI-layers. Incorrectly aligned attachment led to severe degradation of LC switching performance.

Assembly and LC filling of TNC, and Fresnel chamber with SCL platform

Figure 6(a) (later in section 6.1) shows the schematic of the completely assembled VLCF stack with the PCB collars and the SCL platform. The PCB L2 is solder-attached on top of PCB L1. The top electrode of the TNC is attached to the copper pad of PCB L2 and the bottom electrode of the TNC is attached to the bond pad of PCB L1 using an electrically conductive epoxy (MG Chemicals 9410) and cured at 100°C for one hour. The conductivity between the copper bond-pad and the TNC is checked using a multimeter to ensure proper electrical connection. The PCB collar including the electrically connected stack of PCB L1, L2 and the TNC then soldered on to the SCL platform.

Next, for filling the assembled TNC an adequate amount of LC material was dispensed on the TNC holes and like the filling procedure for the Fresnel lens chamber, the TNC assembly was subjected to vacuum filling. Complete filling was observed within 4-5 hours of reaching lowest chamber pressure. The total LC required to fill the TNC chamber was calculated to be 64 nl. After filling, the holes were sealed using very little amount of silicone glue.

Finally, the filled Fresnel chamber is carefully attached to the bottom face of the SCL platform using transparent double-sided Nitto tape, aligned correctly below the TNC stack. A circularly cut linear polarizer of 5 mm (American Polarizers, S-AP42-005T-PSA-12aX19) is attached in front of the TNC. To complete the lens stack, an offset lens of 16.6 D power is then attached on top of the polarizer.

5.3. Optical power and wavefront aberration measurement

A Shack-Hartmann wavefront sensor (SHS) (WFS150-7AR from ThorLabs) and a collimated LED light source (M625L3-C1 from ThorLabs) with wavelength 625 nm were used for measuring VLCF lens optical power and wavefront aberration. The setup is also described in greater details here [6]. All optical measurements were recorded with the lens standing in vertical position. In order to measure the lens' focal length, we utilized the proximity technique [53]. In the proximity technique, the VLCF stack was placed 1 cm apart from the wavefront sensor lenslet array in the vertical direction and the collimated light source was 144 cm apart from the test lens as shown in Fig. 5(a). As the incoming beam into the test lens is collimated, the lens focal length, $f_L = R$ (radius of curvature of incoming light) -L (separation of test lens and sensor). The same setup was utilized for wavefront aberration measurement. We ensured that the outgoing beam from the complete aperture was profiled by SHS for most accurate wavefront aberration measurements. Prior to testing the Fresnel LC lens, the wavefront and optical power of a commercially purchased stock-lens from Edmund optics (LA1401) was first characterized to confirm the accuracy of the test setup. Each lens was extensively characterized and recorded by the SHS system at each stage of device fabrication, i.e., (1) after PDMS curing and peel-off from the mold, (2) assembly of PI-coated glass structures and (3) filling of LC. Lens fabrication was deemed satisfactory only if the SHS output was a near-perfect spherical wavefront, which is typical of spherical lenses. Figure 5(a) shows the experimental setup for performing wavefront and aberration measurements.

5.4. Optical Imaging

Figure 5(b) shows the setup for characterizing the visual perception of images in an imaging system using the fabricated VLCF lens integrated with a Canon camera and a convex offset lens. After filling with LC material, the LC Fresnel lens demonstrates a diverging or concave properties, therefore for proper imaging, an appropriate convex lens (16.67 D) was used to offset the negative power. An aperture of 4 mm is realized using a customized opaque acrylic structure, with a central circular opening of 4 mm. Corresponding to the combined focal length of the Canon camera, VLCF lens and offset convex lens, eye chart and color targets of different sizes were printed on white paper and kept at different distances and lateral positions enabling their simultaneous photography to optically demonstrate the transition between different optical powers of the VLCF lens at different actuation voltages. For demonstration purposes, we performed optical imaging through VLCFs fabricated from Fresnel molds corresponding to both 50D and 25D base-power, and these lenses will henceforth be referred to as VLCF-50 and VLCF-25, respectively. Unless explicitly mentioned, all experimental results correspond to the VLCF-50 lens.

5.5. Tunability characterization of VLCF lens: actuation using varying voltage and duty-cycle

The optical power tunability of the VLCF lens was demonstrated using both the SHS wavefront measurement setup and the imaging setup. The fabricated TNC, filled with LC material was

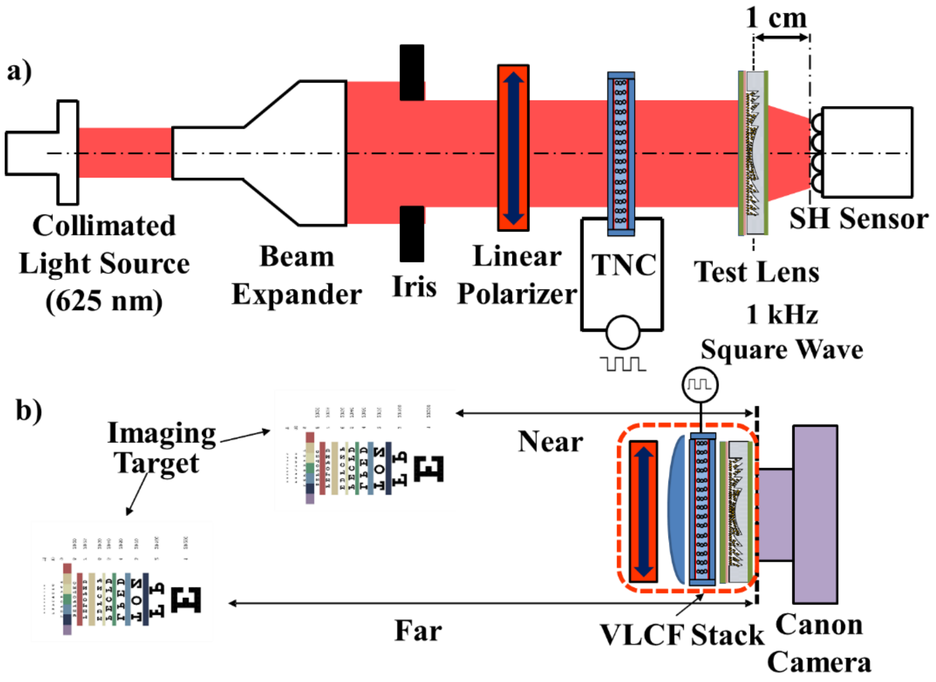

Fig. 5. (a) Setup for measuring focal length measurement and wavefront aberration using SHS. (b) Optical imaging of targets placed at different distances from VLCF stack for demonstrating tunable focus imaging.

electrically connected to a signal generator (Keysight 33500B Series) which provided a square-wave AC signal at a frequency of 1 kHz. The electrical signal was varied using two techniques (1) varying voltage and (2) varying duty-cycle of the square-wave pulse. While it is extremely common to actuate LC lenses using varying voltage, Galstian et al. have demonstrated optical power tuning in LC lens using varying frequency of the input signal whilst keeping the frequency constant [24–26], [48]. In this paper, for the very first time, we demonstrate that LC switching can be also achieved using varying duty-cycle of a square wave AC signal, while keeping its magnitude constant. This approach is advantageous since our final aim is to develop a standalone SCL platform, where there is limited form-factor and voltage signals are controlled using an on-board low-power microcontroller. In such circumstances, it is much easier to vary the duty-cycle in comparison with varying the magnitude of the AC voltage signal. Variable voltage implementations require microcontroller-driven voltage-boosters and precision digital-to-analog converters (DACs) that require additional passive circuitry and electrical power for reliable operation. On the contrary, supplying a constant AC voltage with variable duty-cycle can be achieved using a simple pulse-width-modulation (PWM) module which are usually integrated with typical off-the-shelf microcontroller components, making its implementation more practical for SCL purposes. The TNC was subjected to both voltage and duty-cycle varying square-wave pulses and resulting changes in optical power were measured in the SHS measurement setup and electrical actuation induced variations in plane of focus was recorded using the imaging setup. For the duty-cycle driven experiments, the specific voltage magnitude was decided based on the voltage value which provided the maximum optical power change for the voltage-driven tunability experiments.

5.6. PSF and MTF measurements, and BRISQUE-based image quality assessment

For point spread function (PSF) measurement, the fabricated lens stack (comprising of the VLCF lens, offset lens, TNC and linear polarizer) was illuminated by an expanded and collimated beam from a super-continuum source (SuperK EXTREME EXW-6, NKT Photonics) coupled to a tunable filter (SuperK VARIA, NKT photonics) and the PSF was formed on a monochrome CMOS image sensor (DMM 27UP031- ML, The Imaging Source). More details about the setup can be found here [54]. The PSF of the VLCF stack was measured at the voltage-dependent focal plane for different applied voltages under broadband white-light illumination (λ: 455-755 nm). Furthermore, a typical slant-edge test was also performed to measure the MTF of the fabricated lens at different voltage-dependent focal-planes, when the VLCF stack was subjected to different actuation voltages. The MTF measurements were made using the opensource MTF mapper software. Both the PSF and MTF measurements were taken to characterize the imaging performance of the lens during tunable operation at actuation voltages (a) $< \mathrm{V_T}$ (b) $\sim \mathrm{V_T}$ and (c) $> \mathrm{V_T}$. Where, $\mathrm{V_t}$ is the experimentally determined threshold voltage of the VLCF system. $\mathrm{V_t}$ was considered as the ~average of the range of actuation voltages at which we observed maximum change in optical power of the VLCF system.

In addition to the conventional techniques of characterizing lens performance such as PSF/MTF we believe it is also vital to accurately assess the imaging quality of the VLCF as perceived by the user, since it is primarily designed for SCL applications. This is important since recent approaches to lens design have successfully decoupled the PSF cross-section from lens performance [55]. Therefore, to provide a more holistic characterization of our fabricated LC lenses, we utilize the opensource Python based image assessment machine-learning approach which is a blind/reference-less image spatial quality evaluator (BRISQUE) [56]. Essentially, BRISQUE utilizes image pixels to calculate feature quality by utilizing the principles of spatial Natural Scene Statistics models of locally normalized luminance coefficients in the spatial domain, as well as the model for pairwise products of these coefficients. Images recorded through the lenses were analyzed using the BRISQUE method.

5.7. Comparative assessment of VLCF lenses vs. curved LC lenses

In order to demonstrate the advantage of using refractive Fresnel geometry over traditional approaches for LC applications, a curved refractive lens of the same base power (50D), similarly fabricated and filled with same LC material, was characterized. For providing a comparison between our fabricated VLCF and conventional curved refractive lens, both types of lenses were characterized and compared on the basis of RMS wavefront aberration and BRISQUE analysis. The RMS wavefront aberrations were calculated based on the measurements taken using the SHS system, before and after LC filling for both orthogonal polarizer orientations as well as in the absence of a polarizer. For the BRISQUE analysis, a multi-colored target was imaged using the lenses under both polarizer orientations. This essentially mimics the performance of the lenses operating under voltages smaller and greater than the threshold voltage (V_T).

5.8. Measurement of chromatic aberration in the VLCF lenses

Finally, in order to determine the chromatic aberration (CA) of the VLCF stack, we measured the optical power of a PDMS Fresnel mold and the VLCF lenses under different irradiating source wavelengths in the visible spectrum (450–800 nm) at a measurement period of 5 nm. Different irradiation wavelengths were achieved using a combination of a SuperK Compact white light laser source and SuperK Varia tunable filter. The power of the lens was measured using the Shack Hartmann wavefront sensor for both orthogonal orientations of the polarizer.

6. Results and discussion

6.1. *Fabrication and characterization of tunable lens stack*

Figure 6(a)–(d) shows the schematic of the fabricated VLCF lens stack comprising of the fabricated Offset Lens and linear polarizer (Fig. 6(b)), TNC (Fig. 6(c)), and VLCF lens (Fig. 6(d)) assembled on a multilevel PCB. The thickness of the LC beam-shaping optical elements is 170 µm. However, they are supported by multiple glass frames, each of which are 110 µm thick. Therefore, the final thickness of the entire lens stack is ~1 mm which can be significantly reduced by using much thinner glass frames. The 2D height-profile of the 50D base power Fresnel lens as measured using an Olympus LEXT OLS5000 laser confocal microscope is shown in Fig. 6(e)).

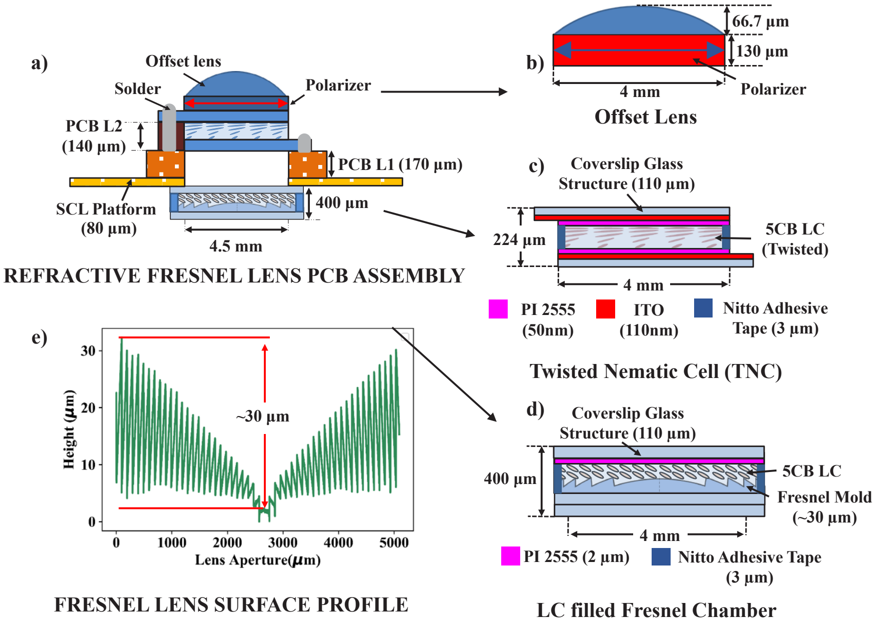

Fig. 6. (a) Schematic of the entire VLCF stack assembled with the flex-PCB SCL platform. (b)–(d) schematic of the individual components of the VLCF stack. (e) Height profile of the Fresnel contour.

Figure 7(a), (b) shows the wavefront and Zernike coefficients of the beam as measured by the SHS after passing through the VLCF before and after LC filling. As shown in the Fig. 7(a), SHS measurements reveal that a typical spherical profile of the wavefront is maintained in both cases, indicating typical wavefront shapes, albeit with opposite focusing abilities. Focal length measurements indicate that the VLCF is a convex lens after fabrication but due to difference in refractive index of PDMS (1.43) and the birefringent 5CB ($n = 1.53–1.71$) [48], it assumes concave characteristics after LC filling. Specifically, the optical power of the VLCF before and after filling was measured to be 30.67 D and -8.9 D, respectively. However, to observe optical power tunability, we need to place a linear polarizer in front of the LC filled Fresnel chamber. Due to the birefringent nature of LC material, the effective optical power of the 5CB filled VLCF lens depends on the relative orientation between the linear polarizer and the director angle of the LC layer. In order to determine the orientation of the polarizer which would yield the greatest tunability, we fixed the VLCF lens and rotated the polarizer about its axis whilst measuring the optical power of the system using the SHS. Rotating the polarizer varied the optical power of the VLCF from a maximum of -9.76 D to a minimum of -15.55 D. The orientation of the polarizer which yielded a net optical power of -9.76 D will be hereby referred to as Polarizer Orientation 1 and rotating the polarizer by 90° about its axis resulted in a net optical power of -15.55 D. It should however be noted that this notation of polarizer direction is rather arbitrary since nearly-symmetric opto-electronic results are obtained by rotating the polarizer by 90°. The Zernike coefficients of the VLCF system also indicated no significant change in aberration measurements before and after LC filling. The maximum difference in RMS wavefront aberrations before and after LC filling was measured to be 0.04 µm, which is significantly lower than the average RMS aberration of the human eye (0.3 µm) [4], [7]. The detailed names of the Zernike coefficients corresponding to the Zernike modes, conforming to *ANSI Standard Z80.28-210* have been provided in Supplement 1 Table S1.

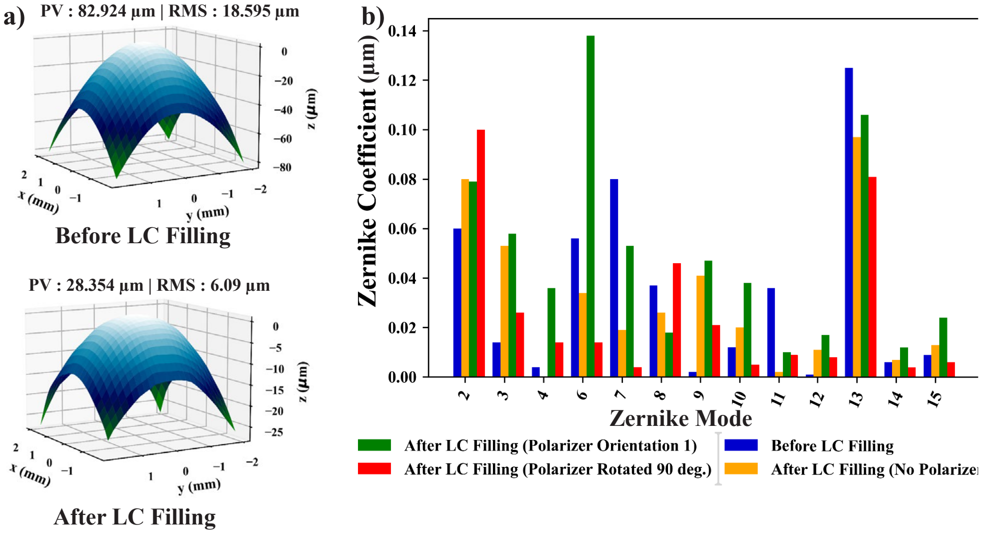

Fig. 7. (a) Wavefront (peak-value (PV) and RMS value) profiles of the VLCF before and after LC filling and (b) aberration coefficients of the Zernike polynomials indicating no significant differences between the coefficients as measured before and after filling of LC material.

The offset lenses with appropriate optical power of 16.67 D were also similarly fabricated. However, this lens provides a static offset to the base power of the lens stack and therefore does not require filling with LC material.

Finally, after complete fabrication of the TNC and assembly with the flexible PCB, continuity tests were performed to ensure proper electrical connectivity. 4-point probe measurements revealed a resistivity of 136 Ω /sq of the ITO layer. Measurements performed using an HP 4284A Precision LCR meter revealed that the capacitance value of the TNC was 0.24 nF at a measurement frequency of 1 kHz.

6.2. Tunability measurements of the VLCF lens

Voltage controlled VLCF lens optical power: Figure 8(a) shows the change in optical power of the VLCF vs. applied V_{RMS} across our fabricated TNC and a commercially purchased polarization rotator from Boldervision [57]. As shown in the plot, an optical power tunability of ~6.5 D was demonstrated by the VLCF when the TNC was subjected to a voltage of 0 - 4 V_{RMS} square-wave AC signal at a frequency of 1 kHz. These results show that the 5CB filled TNC demonstrated a very-low threshold voltage (V_T) of ~2.5 V_{RMS}. This is primarily due to the choice of LC material and the ultra-low thickness of the polyimide layer in the TNC structure. This also resulted in a ~ 248 milli-second response time of the lens. The average power consumption of the lens was ~ 2.6 µWatt. Comparison with the commercial polarization rotator showed that the VLCF driven using our fabricated TNC demonstrated greater tunability. However, the commercial rotator demonstrated perfect unidirectional switching, indicating more controlled alignment of LC molecules. As shown in Fig. 8(b), repeating the experiment after rotating the polarizer by 90° resulted in near-identical mirror-opposite optical power tunability. The very slight asymmetry and bi-directional optical power tunability can be attributed to fabrication errors leading to very slight imperfections in LC molecule alignment. Figure 8(c) shows the comparison plot of maximum tunability of an VLCF lenses versus the base power of the Fresnel lens used for its fabrication (VLCF-10, VLCF-25 and VLCF-50). As expected, a linear correlation between optical power tunability and base power of original mold was observed.

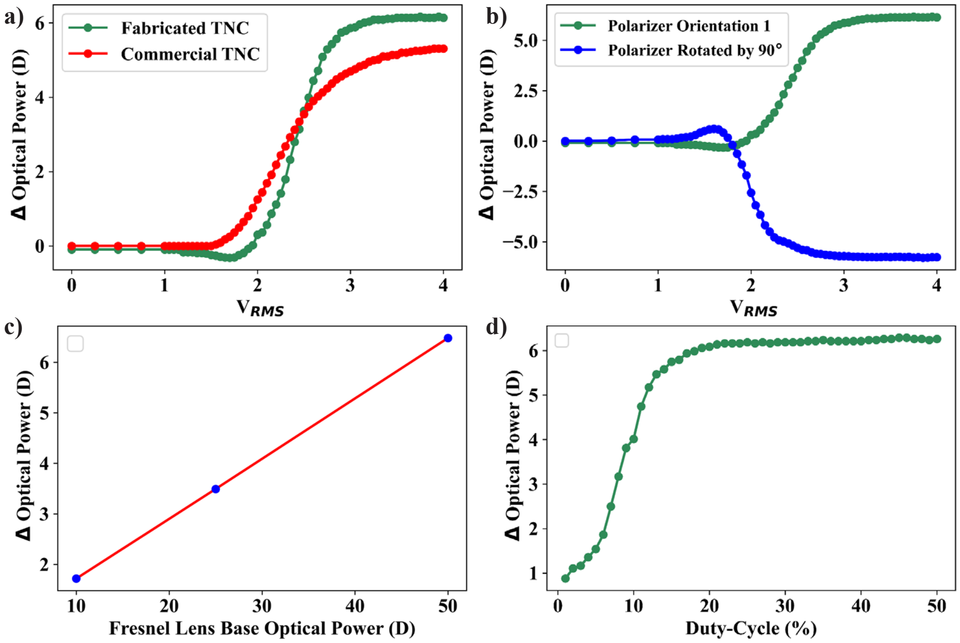

Fig. 8. (a) Change in optical power vs voltage across TNC structures. (b) Change in optical power vs voltage for orthogonal orientations of linear polarizer. (c) Maximum change in optical power vs. base power of Fresnel mold indicating a near linear relationship and (d) change in optical power vs duty-cycle for a fixed voltage of 3.5 V_{RMS}.

Duty-cycle controlled VLCF lens optical power: Figure 8(d) shows the change in optical power of the 50D VLCF lens when our fabricated TNC was subjected to a varying duty-cycle from 0-50%, keeping the AC signal at a constant value of 3.5 V_{RMS}. Results show that the observed optical power tunability was perfectly unidirectional and demonstrated a maximum tunability of ~6.3 D. However, it is interesting to note that the threshold duty-cycle value was only 10% and the maximum tunability was already achieved when the duty-cycle value was varied from 0–20%. This indicates the possible requirement of high-resolution PWM modules for greater control over optical tunability. Like the voltage-driven scenario, rotating the polarizer by 90° resulted in near-identical mirror-opposite optical power tunability. These results demonstrate negligible difference in optical tunability between voltage-driven and duty-cycle driven TNCs and an improved unidirectional behavior in the latter case.

Optical imaging under varying voltage and duty-cycle: Figure 9(a)–(d) shows the optical images of targets placed at different distances from VLCF-25 and VLCF-50, which are biased at voltages lower and greater than the threshold voltage of ~2.5 V_{RMS}. As evident from the figure, varying the voltage results in a smooth transition of focal plane from the target kept close to the lens to that kept far away. As expected, the additional thickness of LC layer for the VLCF-50 lenses leads to lower transmission of white light and increased scattering, thereby reducing the image quality. However, as shown in Fig. 8(c), the optical tunability of the VLCF-50 is $\sim$76% greater than the VLCF-25 lenses. Similarly, Fig. 10(a), (b), which shows the optical imaging performed through VLCF-50, under varying duty cycle of 1% and 50% also demonstrates clear change in focal plane. These results clearly demonstrate that lens can be utilized for varifocal applications and the quality of optical image does not suffer during operation. Visualization 1 and Visualization 2 also show a clear and smooth transition of focal plane under varying voltage and duty-cycle, respectively.

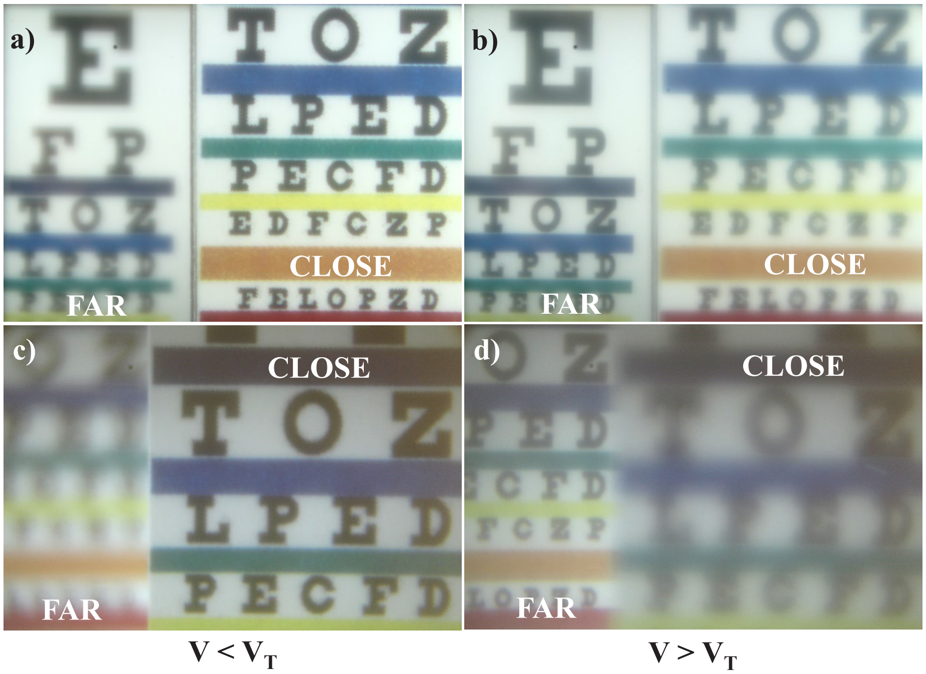

Fig. 9. Optical imaging of multiple targets kept at different distances and imaged through the VLCF lenses fabricated using Fresnel molds of base power (a), (b) 25D and (c), (d) 50D, biased at voltage magnitudes smaller and greater than the threshold voltage of the VLCF system.

6.3. PSF/MTF measurements

The source images of the PSF spot size for all three voltage actuation conditions are shown in Fig. 11(a)–(c). Figure 12(a), (b) shows the normalized intensity plots of the source PSF, for biasing voltages $V < V_T$, $\sim V_T$ and $> V_T$ along both x and y orthogonal directions. As shown in the plot, the intensity distribution displays a very slight lateral displacement during VLCF operation. This is essentially due to asymmetry in molecule orientation or errors in the measurement setup. As shown in Fig. 12(c), the FWHM of the PSF demonstrates a maximum increase of 8.6 μm in the FWHM of the VLCF in the y-direction. Furthermore, slant-edge based MTF measurements (Fig. 12(d)) also demonstrated a negligible change in cut-off frequency during lens operation, with the lowest cut-off spatial frequency of 23.33 lp/mm when the operating voltage was greater than V_T. It is interesting to note that during complete ranges of operation ($V \leq V_T$, $V\sim V_T$ and $V > V_T$) the MTF50 of the lens is equal to that of the average MTF50 for the human eye (at a pupil size of 4 mm), for voltages smaller than or equal to V_T and is only 6 lp/mm

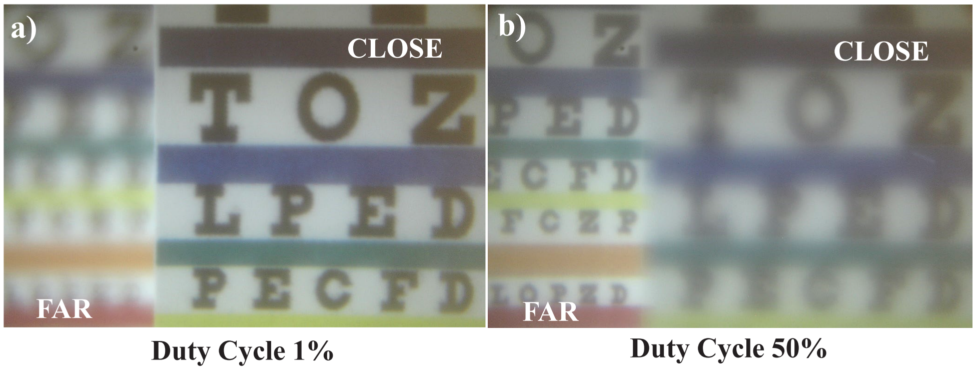

Fig. 10. Optical imaging of multiple targets imaged through the VLCF-50D lens, kept at varying distances under varying (a), (b) duty-cycle.

lesser than that of the human eye for $V > V_T$. Therefore, the PSF/MTF measurements shows that the focusing performance of the VLCF does not suffer any major degradation during the entire range of operation and usage of the VLCF on a human-eye should not cause any significant degradation in imaging quality, thereby demonstrating its potential application for SCL purposes.

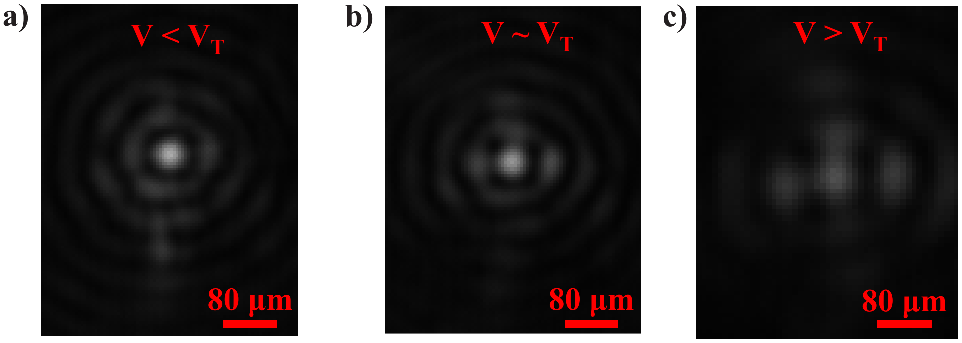

Fig. 11. (a)–(c) source PSF images as recorded by CMOS image sensor.

6.4. Comparative analysis of conventional curved refractive and refractive Fresnel LC lenses

Figure 13(a) shows that the RMS wavefront aberration of the VLCF and curved refractive lens before and after filling of LC material and under different polarizer orientations and without a polarizer. As expected, before LC filling, the conventional lens demonstrates lower RMS wavefront aberration than the Fresnel counterpart. However, after introduction of LC, due to the scattering nature of the liquid-crystal material, the performance of the curved lens degrades considerably. As shown in the bar-plot, after LC filling, the RMS wavefront aberration for the curved lens increases by 15 times for a specific polarizer orientation, which indicates severe degradation of lens performance. Figure 13(b) shows the absolute values of the Zernike coefficients corresponding to the primary Zernike modes. As shown in the plot, the value of Z6 (which corresponds to astigmatism) significantly increases for the curved refractive lens after LC filling, which potentially causes image degradation. A similar conclusion can be drawn by performing BRISQUE analysis of colored target images taken through the VLCF and curved refractive lens (Fig. 14(a)–(d)), after LC filling and under different polarizer orientations. As

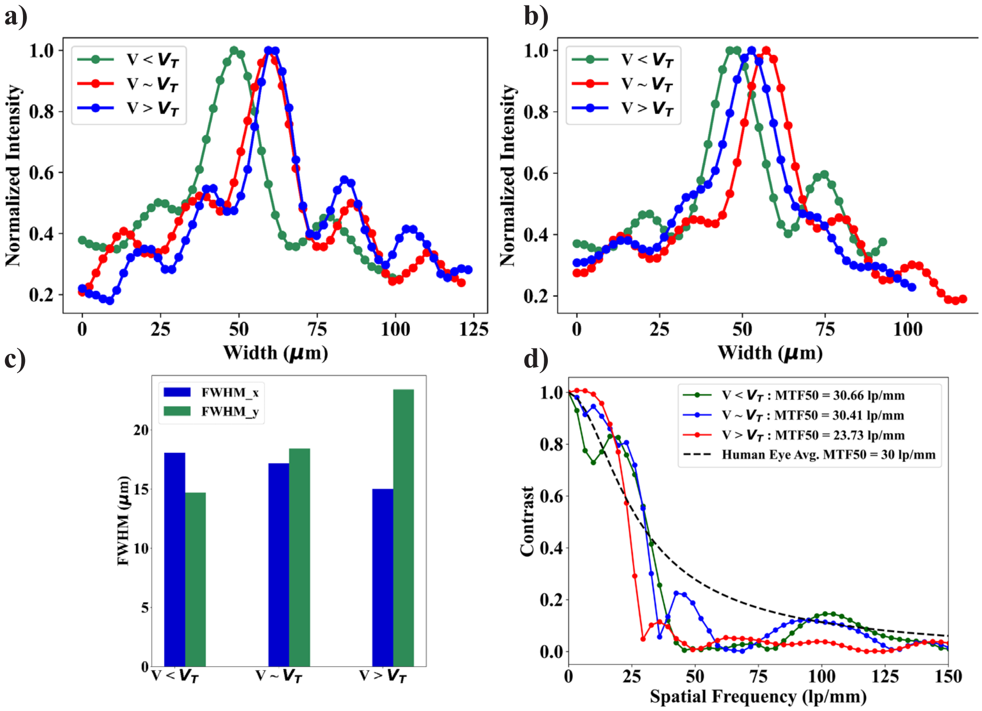

Fig. 12. (a)–(c) Normalized intensity plots and FWHM measurement for the VLCF for V < V_T, ~ V_T and > V_T along orthogonal axes (d) MTF plots showing the cut-off frequency for the VLCF lens for the same voltage ranges and for the human eye.

shown in the figure, the BRISQUE score decreases by ~25 (indicating an improvement in imaging quality) for the VLCF after rotating the polarizer. However, rotating the polarizer results in an increase of ~29 (indicating a degradation in imaging quality) in BRISQUE score for the curved refractive LC lens. Furthermore, the increased thickness of the LC layer also renders the image much darker than the corresponding VLCF lens as shown in (Fig. 14(d)). Aberration measurements and BRISQUE analysis both conclude that for the given tunability and lens aperture requirements, a LC refractive Fresnel optical system will demonstrate an overall better overall imaging performance than a conventional curved LC refractive system, whilst being 88% thinner than its conventional counterpart.

6.5. Chromatic aberration of Fresnel and VLCF lens

For the commercially purchased 50D refractive Fresnel lens (which was used as a mold), the measured optical power ranged from 49.5D – 48.35D, with a standard deviation of 0.38D, when the wavelength of the incident light was varied from 450–800 nm and the CA was measured to be 0.005 D/nm. Measurements performed on the VLCF lens for the same range of incident wavelengths demonstrated a change of -11D – -9D (std. dev of 0.39D) and -12.3D – -11.51D (std. dev of 0.5D) for horizontal and vertical polarizer orientations, respectively. The measured CA for the VLCF was 0.004 and 0.008 D/nm for the orthogonal polarizer orientations, respectively. We believe the CA is adequate for reading and distance applications where a change of 0.5D is barely noticeable to the users.

The measured optical power vs probing wavelength shows oscillations consistent with the steps discussed in the CA calculations of Section 4.1. However, there is a slight mismatch between the predicted and experimentally verified CA values. This is potentially due to errors

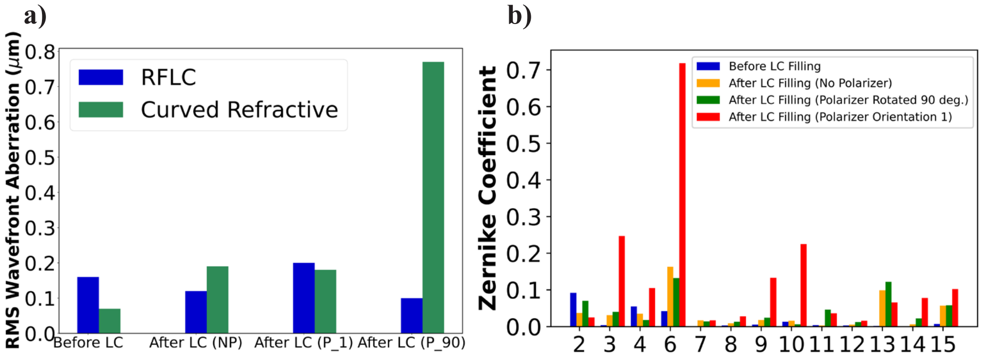

Fig. 13. (a) RMS wavefront aberration measurements taken for the VLCF lens and conventional curved refractive LC lens under different polarizer orientation and (b) absolute Zernike coefficient measurements of the curved LC lens under similar conditions.

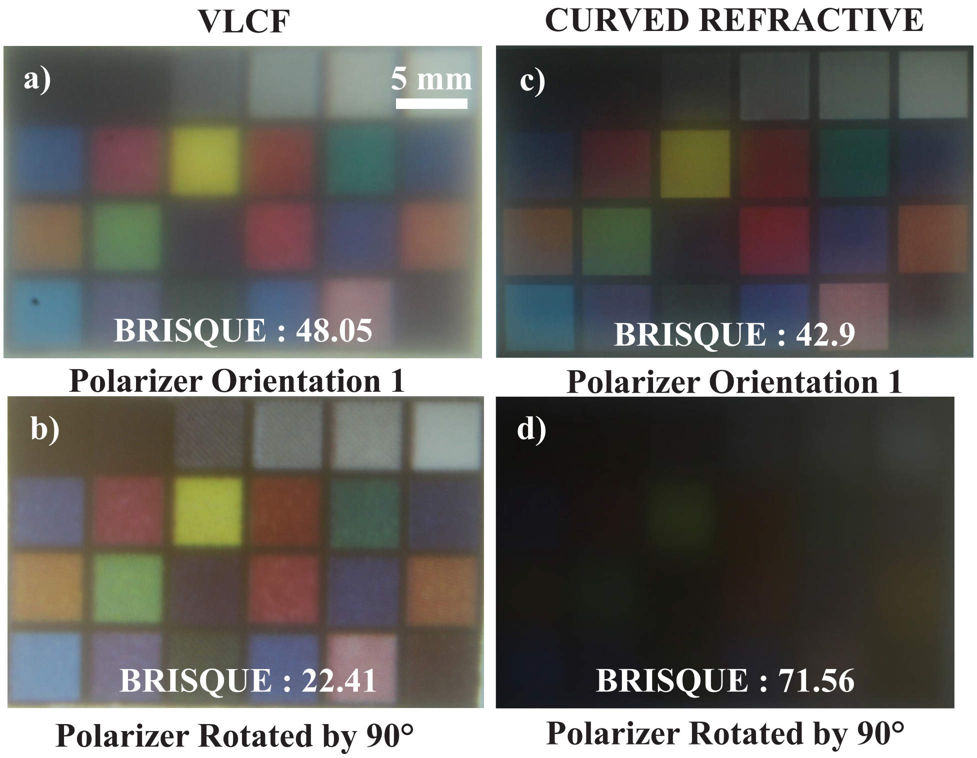

Fig. 14. (a)–(d) Imaging of colored targets and comparative analysis of the imaging performance between VLCF and curved LC lenses using the BRISQUE technique.

in measurement. The limited resolution and lack of precision of the narrow band-pass tunable filter of the probing light-source adds to the errors in measurements. Specifically, we utilize the SuperK Varia tunable filter. The optical specifications of the filter [58] show that the absolute wavelength accuracy is ± 5 nm (error bandwidth of 10 nm). Now, considering the plots in Fig. 2, we see that the slope of the simulated plot of the CA for Fresnel lenses of all orders is ∼ 0.1D/nm. Therefore, one can estimate that the total error per measurement bandwidth of 10 nm is ∼ 1D. This is represented as an error-bar for selected measurement points in Fig. 15. Therefore, the CA for the commercially purchased Fresnel lens is ~0.38 ± 1 D, which lies within the range of the simulated results obtained above (0.87 D).

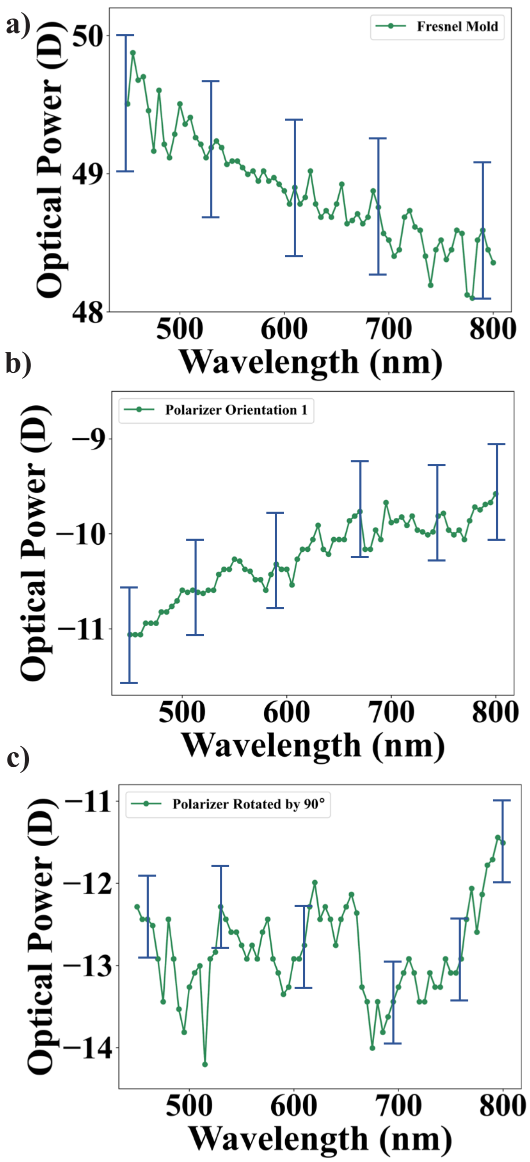

Fig. 15. Chromatic aberration analysis (with estimated error-bar) by measuring optical power vs. wavelength of source light for (a) commercially purchased Fresnel Lens (50D) (b), (c) VLCF lens for orthogonal directions of linear-polarizer.

7. Conclusion

A low-profile and μWatt power consuming tunable focus refractive Fresnel LC lens stack was demonstrated. The total thickness of the beam shaping elements is ~170 μm, the lens has an aperture of ~4 mm, an optical tunability of ~6.5D, response time of ~ 248 milli-seconds and a very-low threshold voltage < 2.5 V_{RMS}. Similar optical tunability was also demonstrated by keeping the voltage constant and by simply varying the duty-cycle of the input AC voltage from

1–50%. The maximum RMS wavefront aberration error was measured to be ~0.2 µm. The FWHM of the PSF and cut-off frequency of the MTF plot remained stable during the entire operation range of the VLCF lens, which demonstrates uniform optical performance of the lens during tunable operation. MTF cut-off frequencies were similar to that of the human eye at 4 mm pupil size, thereby demonstrating that such lenses can be utilized for smart contact lens applications. Comparative analysis demonstrated that the VLCF lens performed better than the traditional curved LC lenses, and at a much-reduced thickness. Maximum std. deviation of measured power vs probing wavelength (chromatic aberration) was ~0.5 D, which is barely noticeable to the human eye. These features of the fabricated VLCF stack make it suitable for low-profile and low-power applications such as a smart-contact lens platform.

Although we have demonstrated a novel, ultra-low power, fast response-time and low-profile VLCF lens system which shows adequate tunability, sufficient for aiding individuals suffering from presbyopia and that can be easily integrated with a smart contact lens platform, there is further scope to improve the imaging quality of the lens. We believe that the primary reasons for imaging defects are substantial scattering due to the thickness of the LC layer and chromatic aberration. To address these issues, one can potentially reduce the size of the aperture, utilize much thinner diffractive lens molds, computationally designed to demonstrate achromatic characteristics.

Funding. National Science Foundation (DMR-1121252, CNS-1932602).

Disclosures. The authors declare no conflicts of interest.

Data availability. Data underlying the results presented in this paper are not publicly available at this time but may be obtained from the authors upon reasonable request.

Supplemental document. See Supplement 1 for supporting content.

References

1. James A Katz, Paul M Karpecki, Alexandra Dorca, Sima Chiva-Razavi, Heather Floyd, Elizabeth Barnes, Mark Wuttke, and Eric Donnenfeld, "Presbyopia – A review of current treatment options and emerging therapies," Clin. Ophthalmol. **15**, 2167–2178 (2021).
2. David A. Goss and Roger W. West, *Introduction to the Optics of the Eye*, 1st Edition (Butterworth-Heinemann, 2001).
3. P. Padmanabhan, C. Zhang, and E. Charbon, "Modeling and analysis of a direct time-of-flight sensor architecture for LiDAR applications," Sensors **19**(24), 1–27 (2019).
4. Mohit U. Karkhanis, Chayanjit Ghosh, Aishwaryadev Banerjee, Nazmul Hasan, Rugved Likhite, Tridib Ghosh, Hanseup Kim, and Carlos H. Mastrangelo, "Correcting Presbyopia with Autofocusing Liquid-Lens Eyeglasses," Jan. (2021).
5. Nazmul Hasan, Aishwaryadev Banerjee, Hanseup Kim, and Carlos H. Mastrangelo, "Tunable-focus lens for adaptive eyeglasses," Opt. Express **25**(2), 1221 (2017).
6. Nazmul Hasan, Aishwaryadev Banerjee, Hanseup Kim, and Carlos H. Mastrangelo, "A Low-Power Light-Weight Tunable Lens for Ophthalmic Applications," in *Imaging and Applied Optics* (2016), paper AOM3C.4.
7. Mohit U. Karkhanis, Aishwaryadev Banerjee, Chayanjit Ghosh, Rugved Likhite, Erfan Pourshaban, Hanseup Kim, David A. Meyer, and Carlos H. Mastrangelo, "Compact Models of Presbyopia Accommodative Errors for Wearable Adaptive-Optics Vision Correction Devices," IEEE Access **10**, 68857–68867 (2022).
8. A. Vásquez Quintero, H. Pérez-Merino, and De Smet, "Artificial iris performance for smart contact lens vision correction applications," Sci. Rep. **10**(1), 14641 (2020).
9. Lyndon Jones, Alex Hui, Chau-Minh Phan, Michael L Read, Dimitri Azar, John Buch, Joseph B Ciolino, Shehzad A Naroo, Brian Pall, Kathleen Romond, Padmaja Sankaridurg, Cristina M Schnider, Louise Terry, and Mark Willcox, "CLEAR - Contact lens technologies of the future," Contact Lens Anterior Eye **44**(2), 398–430 (2021).
10. Do Hee Keum, Su-Kyoung Kim, Jahyun Koo, Geon-Hui Lee, Cheonhoo Jeon, Jee Won Mok, Beom Ho Mun, Keon Jae Lee, and Ehsan Kamrani, "Wireless smart contact lens for diabetic diagnosis and therapy," Sci. Adv. **6**(17), eaba3252 (2020).
11. Shinya Kusama, Kaito Sato, Shotaro Yoshida, and Matsuhiko Nishizawa, "Self-Moisturizing Smart Contact Lens Employing Electroosmosis," Adv. Mater. Technol. **5**(1), 1900889 (2020).
12. Chayanjit Ghosh, Alex Mastrangelo, Mohit Karkhanis, Adwait Deshpande, Aishwaryadev Banerjee, Hanseup Kim, and Carlos H Mastrangelo, "Low-Profile Induced-Voltage Distance Ranger for Smart Contact Lenses," IEEE Trans. Biomed. Eng. **68**(7), 2203–2210 (2020).
13. Chayanjit Ghosh, Sakthidasan Kalidasan, Mohit U. Karkhanis, Alex Mastrangelo, Aishwaryadev Banerjee, Ross Walker, Hanseup Kim, and Carlos H. Mastrangelo, "A Nano-Joule Burst-Mode Eye-Gaze Angle and Object Distance Sensor for Smart Contact Lenses," in *2021 IEEE Sensors* (2021), pp. 1–4.

14. Chayanjit Ghosh, Alex Mastrangelo, Aishwaryadev Banerjee, Hanseup Kim, and Carlos H. Mastrangelo, "Micropower Object Range and Bearing Sensor for Smart Contact Lenses," in *2020 IEEE Sensors* (2020), pp. 1–4.
15. Erfan Pourshaban, Aishwaryadev Banerjee, Adwait Deshpande, Chayanjit Ghosh, Mohit U. Karkhanis, Rabiul Hasan, Nathan D. Rock, Hanseup Kim, and Carlos H. Mastrangelo, "Flexible and Semi-Transparent Silicon Solar Cells as a Power Supply to Smart Contact Lenses," ACS Appl. Electron. Mater. **4**(8), 4016–4022 (2022).
16. Erfan Pourshaban, Aishwaryadev Banerjee, Mohit U. Karkhanis, Adwait Deshpande, Chayanjit Ghosh, Hanseup Kim, and Carlos H. Mastrangelo, "Eye Tear Activated Mg-Air Battery Driven by Natural Eye Blinking for Smart Contact Lenses," Adv. Mater. Technol. **8**(1), 2200518 (2023).
17. Erfan Pourshaban, Adwait Deshpande, Mohit U. Karkhanis, Aishwaryadev Banerjee, Chayanjit Ghosh, Hanseup Kim, and Carlos H. Mastrangelo, "A Micro-Fabricated Aluminum-Air Moving Biofluid Battery for Medical Wearables," in *IEEE Symposium on Mass Storage Systems and Technologies* (2022), pp. 608–611.
18. Erfan Pourshaban, Mohit U. Karkhanis, Adwait Deshpande, Aishwaryadev Banerjee, Chayanjit Ghosh, Hanseup Kim, and Carlos H. Mastrangelo, "A Magnetically-Coupled Micromachined Electrostatic Energy Harvester Driven by Eye Blinking Motion," in *21st International Conference on Solid-State Sensors, Actuators and Microsystems (Transducers)* (2021), pp. 960–963.
19. Erfan Pourshaban, Aishwaryadev Banerjee, Chayanjit Ghosh, Adwait Deshpande, Hanseup Kim, and Carlos H. Mastrangelo, "Semi-transparent and Flexible Single Crystalline Silicon Solar Cell," in *48th Photovoltaic Specialists Conference* (IEEE, 2021), pp. 1897–1900.
20. Aishwaryadev Banerjee, Chayanjit Ghosh, Mohit Karkhanis, Erfan Pourshaban, Hanseup Kim, and Carlos H. Mastrangelo, "Low-power, thin and flexible, stacked digital LC lens for adaptive contact lens system with enhanced tunability," *Conf. Lasers Electro-Optics* (2021), pp. 8–9.
21. Aishwaryadev Banerjee, Chayanjit Ghosh, Mohit Karkhanis, Adwait Deshpande, Erfan Pourshaban, Hanseup Kim, and Carlos H. Mastrangelo, "Microfabricated Low-Profile Tunable LC-Refractive Fresnel (LCRF) Lens for Smart Contacts," in *Conference on Lasers and Electro-Optics* (2022), paper AW4C.3.
22. Y. H. Lin, Y. J. Wang, and V. Reshetnyak, "Liquid crystal lenses with tunable focal length," Liq. Cryst. Rev. **5**(2), 111–143 (2017).
23. H. C. Lin, M. S. Chen, and Y. H. Lin, "A review of electrically tunable focusing liquid crystal lenses," Trans. Electr. Electron. Mater. **12**(6), 234–240 (2011).
24. S. M. Kelly and M. O'Neill, "Liquid crystals for electro-optic applications," in *Handbook of Advanced Electronic and Photonic Materials and Devices*, H. Singh Nalwa, ed. (Academic Press, 2001), Chapter 1 pp. 1–66.
25. F. J. Kahn, "Electric-field-induced orientational deformation of nematic liquid crystals: Tunable birefringence," Appl. Phys. Lett. **20**(5), 199–201 (1972).
26. R. A. Soref and M. J. Rafuse, "Electrically controlled birefringence of thin nematic films," J. Appl. Phys. **43**(5), 2029–2037 (1972).
27. T. Galstian, K. Asatryan, V. Presniakov, A. Zohrabyan, A. Tork, A. Bagramyan, S. Careau, M. Thiboutot, and M. Cotovanu, "High optical quality electrically variable liquid crystal lens using an additional floating electrode," Opt. Lett. **41**(14), 3265 (2016).
28. O. Sova and T. Galstian, "Liquid crystal lens with optimized wavefront across the entire clear aperture," Opt. Commun. **433**, 290–296 (2019).
29. L. Begel and T. Galstian, "Liquid crystal lens with corrected wavefront asymmetry," Appl. Opt. **57**(18), 5072 (2018).
30. T. Galstian and A. Pusenkova, "Light scattering by liquid crystals and its impact on adaptive imaging," Proc. SPIE **11472**, 114720X (2020).
31. A. Pusenkova and T. Galstian, "Reducing the light scattering impact in liquid-crystal-based imaging systems," Appl. Opt. **59**(16), 4780 (2020).
32. Harry E. Milton, Philip B. Morgan, John H. Clamp, and Helen F Gleeson, "Electronic liquid crystal contact lenses for the correction of presbyopia," Opt. Express **22**(7), 8035 (2014).
33. J Bailey, S Kaur, P B Morgan, H F Gleeson, J H Clamp, and J C Jones, "Design considerations for liquid crystal contact lenses," J. Phys. D: Appl. Phys. **50**(48), 485401 (2017).
34. I. Dror, A. Sandrov, and N. S. Kopeika, "Experimental investigation of the influence of the relative position of the scattering layer on image quality: the shower curtain effect" (1998).
35. A. Vijayakumar and S. Bhattacharya, *Design and Fabrication of Diffractive Optical Elements with MATLAB* (SPIE, 2017).
36. D. W. Sweeney and G. E. Sommargren, "Harmonic diffractive lenses," Appl. Opt. **34**(14), 2469 (1995).
37. S. Sato, A. Sugiyama, and R. Sato, "Variable-Focus Liquid-Crystal Fresnel Lens," Jpn. J. Appl. Phys. **24**(8A), L626 (1985).
38. Shiyao Li, Wenwen Wang, Yongai Zhang, Qun Yan, Tailiang Guo, Xiongtu Zhou, and Chaoxing Wu, "Electrically tunable large aperture liquid crystal lens with dual hole-patterned electrodes," Opt. Commun. **510**, 127911 (2022).
39. Y. H. Hsu, B. Y. Chen, and C. R. Sheu, "Improvement of Hole-Patterned Electrode Liquid Crystal Lens by Coplanar Inner Ring Electrode," IEEE Photonics Technol. Lett. **31**(20), 1627–1630 (2019).
40. S. Sato, T. Nose, R. Yamaguchi, and S. Yanase, "Relationship between lens properties and director orientation in a liquid crystal lens," Liq. Cryst. **5**(5), 1435–1442 (1989).
41. James Bailey, Philip B. Morgan, Helen F. Gleeson, and J. Cliff Jones, "Switchable liquid crystal contact lenses for the correction of presbyopia," Crystals **8**(1), 29 (2018).

42. James Bailey, John Clamp, Steven Farmer, Helen F Gleeson, Tim Haynes, J Cliff Jones, Tom Moorhouse, and Philip Morgan, "Infrared triggered smart contact lens for the treatment of presbyopia," J. Phys. D: Appl. Phys. **55**(21), 210001 (2022).
43. S. Sato, "Liquid-crystal lens-cells with variable focal length," Jpn. J. Appl. Phys. **18**(9), 1679–1684 (1979).
44. T. R. M. Sales and G. M. Morris, "Diffractive–refractive behavior of kinoform lenses," Appl. Opt. **36**(1), 253 (1997).
45. Jianming Yang, Patrice Twardowski, Philippe Gérard, Wenhui Yu, and Joël Fontaine, "Chromatic analysis of harmonic Fresnel lenses by FDTD and angular spectrum methods," Appl. Opt. **57**(19), 5281 (2018).
46. H. H. Hopkins, "The frequency response of a defocused optical system," Proc. R. Soc. Lond. A **231**(1184), 91–103 (1955).
47. "Fresnel Lenses-Edmund Optics," https://www.edmundoptics.com/f/fresnel-lenses/12434/.
48. J. Li and S. T. Wu, "Two-coefficient Cauchy model for low birefringence liquid crystals," J. Appl. Phys. **96**(1), 170–174 (2004).
49. Marjorie Senechal, *Shaping Space* (Springer, 2013).
50. Dowon Ahn, Yong-Cheol Jeong, Seungwoo Lee, Jihye Lee, Yongjoon Heo, and Jung-Ki Park, "Control of liquid crystal pretilt angles by using organic/inorganic hybrid interpenetrating networks," Opt. Express **17**(19), 16603 (2009).
51. A. Banerjee, R. Likhite, H. Kim, and C. H. Mastrangelo, "Quantum Tunneling Hygrometer with Temperature Stabilized Nanometer Gap," Sci. Rep. **10**(1), 4440 (2020).
52. Rugved Likhite, Aishwaryadev Banerjee, Apratim Majumder, Mohit Karkhanis, Hanseup Kim, and Carlos H. Mastrangelo, "VOC sensing using batch-fabricated temperature compensated self-leveling microstructures," Sens. Actuators, B **311**, 127817 (2020).
53. Daniel R. Neal, R. James Copland, David A. Neal, Daniel M. Topa, and Phillip Riera, "Measurement of lens focal length using multi-curvature analysis of Shack-Hartmann wavefront data" (2022).
54. M. Meem, A. Majumder, and R. Menon, "Free-form broadband flat lenses for visible imaging," OSA Contin. **4**(2), 491 (2021).
55. Apratim Majumder, Monjurul Meem, Robert Stewart, and Rajesh Menon, "Broadband point-spread function engineering via a freeform diffractive microlens array," Opt. Express **30**(2), 1967 (2022).
56. A. Mittal, A. K. Moorthy, and A. C. Bovik, "No-reference image quality assessment in the spatial domain," IEEE Trans. Image Process. **21**(12), 4695–4708 (2012).
57. "TWISTED NEMATIC (TN) LIQUID CRYSTAL ROTATOR," https://boldervision.com/product/twisted-nematic-tn-liquid-crystal-rotator/.
58. "SuperK VARIA tunable filter," https://www.nktphotonics.com/products/supercontinuum-white-light-lasers/superk-varia/.